Princeton Plasma Physics Laboratory

PPPL-4000rev

PPPL-4000rev

# Microturbulent Drift Mode Stability before Internal Transport Barrier Formation in the Alcator C-Mod Radio Frequency Heated H-mode

M.H. Redi, W. Dorland, C.L. Fiore, J.A. Baumgaertel,
E.M. Belli, T.S. Hahm, G.W. Hammett, and G. Rewoldt

August 2004
Revised May 2005

PPPL
PRINCETON PLASMA
PHYSICS LABORATORY

Prepared for the U.S. Department of Energy under Contract DE-AC02-76CH03073.

## PPPL Reports Disclaimer



## Availability

This report is posted on the U.S. Department of Energy's Princeton Plasma Physics Laboratory Publications and Reports web site in Fiscal Year 2004. The home page for PPPL Reports and Publications is: http://www.pppl.gov/pub_report/

DOE and DOE Contractors can obtain copies of this report from:

U.S. Department of Energy
Office of Scientific and Technical Information
DOE Technical Information Services (DTIS)
P.O. Box 62
Oak Ridge, TN 37831

Telephone: (865) 576-8401

Fax: (865) 576-5728

Email: reports@adonis.osti.gov

This report is available to the general public from:

National Technical Information Service
U.S. Department of Commerce
5285 Port Royal Road
Springfield, VA 22161

Telephone: 1-800-553-6847 or
(703) 605-6000

Fax: (703) 321-8547

Internet: http://www.ntis.gov/ordering.htm

# Microturbulent drift mode stability before internal transport barrier formation in the Alcator C-Mod radio frequency heated H-mode

M. H. Redi

*Princeton Plasma Physics Laboratory, Princeton, NJ 08543, USA*

W. Dorland

*Institute for Plasma Research, U. MD, College Park, MD 20742, USA*

C. L. Fiore

*Plasma Science and Fusion Center, MIT, Cambridge, MA 02139, USA*

J. A. Baumgaertel, E. M. Belli, T. S. Hahm, G. W. Hammett, G. Rewoldt

*Princeton Plasma Physics Laboratory, Princeton, NJ 08543, USA*

(Received

H-mode experiments on Alcator C-Mod [I. H. Hutchinson, *et al.*, Phys. Plas. **1**, 1511 (1994)] which exhibit an internal transport barrier (ITB) have been examined with gyrokinetic calculations, before barrier formation. Ion temperature gradient (ITG) and electron temperature gradient (ETG) modes are unstable outside the barrier region and not strongly growing in the core; in the barrier region ITG is only weakly unstable. Linear calculations support the picture that ITG and ETG modes drive high transport outside the ITB, and that weakly unstable ITG modes in the barrier region correlate with reduced particle transport and improved thermal confinement even before the ITB is established, without the need for ***ExB*** shear stabilization. Long wavelength mode stability in the barrier region is analyzed in the context of a phase diagram for ion and electron drift waves by varying the temperature and density scale lengths. Results from the gyrokinetic code GS2 [M. Kotschenreuther, *et al.*, Comp. Phys. Comm. **88,** 128

(1995)] are compared to standard threshold models and benchmark successfully against experiment in the plasma core.

(PACS numbers: 52.30.Gz, 52.35Kt, 52.35Qz, 52.35.Ra, 52.55.F)

## I. INTRODUCTION

When internal barriers to plasma particle and energy transport develop, high temperature plasma is well confined, a necessary step toward economical fusion reactors. Because Alcator C-Mod[1] is a toroidal magnetic confinement device with high toroidal field, high plasma density, and radio frequency (rf) heating, its transport characteristics are of special interest, being relevant to fusion reactor scenarios[2]. In this paper, plasma conditions just before internal transport barrier (ITB) formation on C-Mod are analyzed for linear drift mode stability using the GS2[3,4] gyrokinetic code. This code provides a stability analysis of ion temperature gradient (ITG), trapped electron mode (TEM) and electron temperature gradient (ETG) drift modes using a fully electromagnetic, flux-tube model, four plasma species, a realistic numerical equlibrium, electron and ion collisions and including the full nonadiabatic electron response.

The paper is organized as follows: in Sec. II we describe the experimental conditions; in Sec. III the gyrokinetic equations and analysis results are presented, including extensive linear studies of the effects of density and temperature scale length changes on ITG/TEM stability. In the discussion of Sec. IV, code results are compared to standard models and tested against transport analysis of the experiment. The paper concludes with a summary in Sec. V.

## II. ALCATOR C-MOD INTERNAL TRANSPORT BARRIER EXPERIMENT

Following off-axis rf heating and establishment of a high performance (H-mode) plasma, C-Mod develops a reproducible ITB with a steep electron density profile[5]. In contrast to other such experiments[6], this ITB occurs without reversed magnetic shear or high plasma rotation. This experiment is the subject of much recent analysis[5,7-16], including gyrokinetic simulations[14] of strong TEM microturbulence late in the discharge, during the fully developed ITB phase. These ITB experiments are of special interest as thermal confinement found from experimental

transport analysis is higher than predicted by neoclassical theory in the plasma core. A typical such experiment is analyzed here, pulse #1001220016 (Fig. 1). This experiment is characterized by $R_o$= 0.69 m, $B_o$= 4.5 T, $I_p$=0.78 MA, and central electron density $n_e(0)$= 4x$10^{20}$/$m^3$, where the majority ions are deuterium. The central plasma beta, defined as the plasma kinetic energy at the magnetic axis divided by the confining field magnetic energy, is less than 1%. Toroidal rotation is found to reverse sign as the barrier is established, being near zero at the plasma center at the time of ITB onset (Fig. 1).

The ITB exhibits steep, spontaneous density peaking and a reduction in particle transport occurring without a central particle source. The ITB develops in the early phase of a dual frequency rf experiment, with central rf heating providing density control later in the discharge. In the early phase, an ion cyclotron radio frequency (ICRF) EDA H-Mode, the hydrogen minority resonance is at $r/a$~0.5 on the high field side, beginning at 0.7 s. EDA refers to enhanced $D_\alpha$ radiation, which characterizes high performance H-modes at high densities and temperatures. Plasma radii are normalized by the midplane half radius, $a$ = 0.22 m. ITBs form in both ohmic and ICRF heated plasmas, from fully equilibrated H-modes. Modeling of radio frequency heating of the hydrogen minority indicates the hydrogen temperature ($T_h=2E_h/3k$) to be peaked around the half radius, with a less radially peaked hydrogen density profile. The ion distribution function is not thought to have a high energy rf tail, due to the high density and collisionality.

The density profile data was obtained from inverted visible bremstrahlung measurements, adjusted for the $Z_{eff}$ and temperature dependence. Electron temperature data was taken from Thomson scattering as the electron cyclotron emission (ECE) signal is cut off during the ITB because of rising electron density.

Ion and electron collisions have a strong impact on drift wave stability and depend sensitively on plasma densities and temperatures. Consequently, the identification of impurities and characterization of minority species is important in microstability modeling. The impurity and minority ions at 0.9 s are estimated to be 3% boron and 4% hydrogen. The walls of C-Mod are molybdenum, regularly coated with boron (from $D_2B_6$ boronization) for edge density control. Examination of bolometer profiles indicates molybdenum levels less than 0.1%. The low-$Z$ impurity level is estimated at 3% from visible bremsstrahlung measurements, yielding $Z_{eff}$~1.64. The impurity ion is identified as boron, although the low-$Z$ impurities may be actually 2% boron and 1% carbon. Boron and carbon are so similar in collisional properties that only boron impurity ions are included in the calculations. No oxygen is thought to have been present. The hydrogen to deuterium ratio, 4% at 0.9 s, was obtained from spectroscopic measurements of $D_\alpha$ and $H_\alpha$ radiation.

Error in the experimental measurements of all data is estimated to be on the order of 10-20%. The experimental data was analyzed with the TRANSP code[17]. The plasma ion temperature profile in TRANSP was modeled under the assumption that $\chi_i$ is proportional to the neoclassical ion diffusivity[18], $\chi_i = K\chi_i^{Chang\text{-}Hinton}$. The factor of proportionality, $K$, is chosen to match the measured neutron data at the plasma center to that computed by TRANSP in the transport analysis. $K$ varies during the evolution of the plasma, being about 1.5 when averaged over 0.85 to 0.95 s. This leads to $T_i(r)$ being broader, and slightly lower than $T_e(r)$. While the high density of C-Mod suggests that $T_i = T_e$ would be a good assumption in the plasma core, the data are consistent with either ion thermal loss model[8].

Radial profiles of the electron density, the magnetic safety factor $q$, the electron temperature and the ion temperature from the TRANSP analysis for times within the L-mode, H-

mode and early ITB phases are shown in Fig. 2. This analysis included a sawtooth model which causes the safety factor to drop below unity by ~10% at each sawtooth. As the sawtooth period is 10 ms, a sawtooth-averaged condition is used for the gyrokinetic calculations. TRANSP modeling leads to a normal shear profile, with $q$ monotonic. Three radial locations ($r/a$=0.25, 0.45, 0.65) were chosen for microstability analyses to characterize the core, barrier region and outer plasma conditions. The times of interest chosen for the gyrokinetic calculations near the time of ITB onset are 0.8 s and 0.9 s.

The TRANSP results were processed with TRXPL[19], averaging over 50 ms at the time of interest. TRXPL generates the input files for the microstability calculations, recomputing the plasma equilibrium and calculating the input parameters for the gyrokinetic code from the TRANSP profiles of the plasma densities, temperatures, *etc*. These parameters are given in Table I. In these calculations the ratios of the deuterium, boron and hydrogen ion densities to the electron density are $n_d/n_e$ = 0.8, $n_b/n_e$ = 0.03, $n_h/n_e$ = 0.04. The normalizations for reference mass and reference length are $m_{ref}$ = 2 and $a_{ref}$ = 0.22 m. The electron, deuterium, boron and hydrogen ion collisionalities, $\nu_{e\text{-}i}$, $\nu_{d\text{-}i}$, $\nu_{b\text{-}i}$, $\nu_{h\text{-}i}$, are defined at the GS2 webpage[4]. Mode growth rates and real frequencies are usually normalized in physical units, $c_s/a$. The normalization $c_s/a$ for each radius is specified in laboratory units (MHz) in Table I; the electron thermal velocity is defined $v_{te}=(T_e/m_e)^{0.5}$.

## III. GYROKINETIC CALCULATIONS

### A. Gyrokinetic model of drift wave turbulence

The transport of particles and energy in high temperature fusion plasmas is widely believed to result from the turbulence of drift wave fluctuations (see Wesson[20] and references therein). Three types of drift waves are believed to affect plasma confinement: the ion

temperature gradient (ITG) mode[20,21], the trapped electron mode (TEM)[20-22], and the electron temperature gradient (ETG) mode driven by passing electrons[4,23-26]. The longest wavelength drift mode microturbulence in our study is characterized by normalized wave vectors, $0.1 \le k_\perp \rho_s \le 1$, where $\rho_s \equiv \sqrt{m_d T_e / eB}$ and $k_\perp$ is the wave vector component perpendicular to the magnetic field line which wraps around a magnetic flux surface. We denote instabilities at these wavelengths "ITG/TEM" as they are often hybrid modes characterized by both ITG and TEM behavior. The trapped ion mode (TIM) turbulence[20,27] which corresponds to even longer wavelengths has typically lower linear growth rate and is not considered in these linear stability studies. For $1 \le k_\perp \rho_s \le 10$ the instabilities are again designated ITG/TEM, transitioning to pure ETG microturbulence above $k_\perp \rho_s \sim 10$.

Because the ITG/TEM mode has the longest wavelength, it is most likely to cause plasma transport. In this paper we consider all drift mode instabilities at the onset time, but particularly investigate whether the experiment is above or below marginal stability of the ITG/TEM for $0.1 \le k_\perp \rho_s \le 1$, and compare the ITGTEM critical temperature gradient to standard models used in reactor design.

In general, driving forces for the microturbulence arise from temperature and density gradients in $\omega_{*s}$, mediated by the effects of passing ions and of trapped electrons. Stabilization of turbulence can be achieved through high values of magnetic shear $\hat{s}$, $q$, $\beta' = \nabla\beta$, impurities, collisional effects, and nonzero $T_e$. See references 20 and 21 for detailed discussion and additional citations about the plasma physics which underlies these effects. The competition among many driving and stabilizing forces requires computational methods to analyse a particular experimental situation.

Calculations were carried out on the Department of Energy National Energy Research Scientific Computing Center's IBM RS/6000SP computer with 64 parallel processors distributed on 4 nodes, using approximately 5,000 hours of computation on the IBM SP. The gyrokinetic Vlasov-Maxwell system equations described above are iteratively solved for 10,000-50,000 time steps, until the microinstability growth rates, $\gamma$, and real frequencies, $\omega$, are verified to have converged and the usual measure of the electrostatic potential, $ln|\phi|^2$, is verified to be linearly increasing, in cases designated unstable.

### B. Gyrokinetic calculations of ITG/TEM at 0.8 and 0.9 s

On C-Mod, ITBs generally develop from fully equilibrated H-modes. A linear stability analysis was carried out for the ITB region early in the H-mode phase at 0.8 s and in the fully equilibrated H-mode at 0.9 s, just before ITB onset. The calculations are intended to understand the conditions before ITB formation, and possibly to identify a trigger mechanism. At 0.8 s and at 0.9 s the input plasma parameters are the same within 10%, except $|a_{ref}\nabla n_j/n_j|$ which is ~0.07 at 0.8 s, rather than ~0.42, for all species $j$. The long wavelength growth rate and real frequency spectra of weak, fully converged ITG/TEM modes at 0.8 s and 0.9 s are very similar (Fig. 3) as are those for the higher wavelength ITG/TEM and ETG drift modes. All subsequent calculations in this paper concern plasma conditions at 0.9 s in the fully equilibrated H-mode phase or variations about those conditions.

### C. Gyrokinetic calculations for ITG/TEM and ETG drift modes at 0.9 s

Figure 4 depicts a phase diagram for long wavelength drift mode instability, adapted from Fig. 1 of Ref. 28. In it we map the stability analysis results for the experimental radii at the onset time (Fig. 5) and for variations in the temperature and density gradients of the plasma species (discussed in Sec. IIID). We keep the ITG and TEM labels of Ref. 28 for this figure. Star

symbols indicate the three C-Mod radial locations simulated, with stable conditions found in the plasma core (red) and weakly unstable ITG modes at the barrier region (green) and strongly unstable ITG modes outside the barrier region (blue). Dashed lines represent the coordinates for calculated variations about the base case at the barrier region, in the two-dimensional, normalized temperature gradient and density gradient space. For Fig. 1 of Ref. 28, it is assumed that $\beta$ is low, $T_e=T_i$ and that ETG modes are not unstable; in contrast the calculations for the C-Mod experiment show ETG unstable. We define $R\nabla T/T \equiv (R\nabla T_i/T_i+R\nabla T_e/T_e)/2$ and $R\nabla N/N \equiv (R\nabla n_d/n_d +R\nabla n_e/n_e)/2$. $R$ is the plasma major radius. The microstability analysis paths depicted in Fig. 4 by dashed lines track transitions from stable to unstable conditions as well as between the ITG and TEM instabilities, as discussed below.

Figures 5a and 5c show the wave vector dependent spectra of drift mode growth rates and real frequencies, respectively, at the ITB onset time, 0.9 sec for each radius, on a log abscissa. Fig. 5b shows the ITG/TEM growth rates on a linear abscissa.

In the plasma core ETG modes are stable**.** In the core, weakly unstable ITG/TEM modes, apparently well converged in time, with $0.3< k_\perp\rho_s <0.6$ (0.02 MHz) are found in calculations of five $2\pi$ field periods along the field line. These instabilities, possibly driven by boundary conditions and the breakdown of the ballooning approximation for very low magnetic shear, have very low growth rates (<0.005 MHz) for field lines extended to seventeen $2\pi$ field periods. They rotate in the electron diamagnetic direction with peaks in the eigenfunctions from particle trapping regions in each period. Convergence studies in field line length were necessary in the plasma core, but not at or outside the ITB region, due to the good eigenfunction localization there. The ITG/TEM instability is not expected in the plasma core, since $\eta^i \equiv (\nabla T_i/T_i)/(\nabla n_e/n_e)$=0.94. These modes are unlikely to be kinetic ballooning instabilities since

$\beta$=0.75% in the plasma core. The modes in the plasma core are probably spurious, arising from inadequate box size, and were not pursued further. We conclude that there are no strongly growing unstable ITG/TEM drift modes in the plasma core. The core growth rates and real frequencies for ITG/TEM modes are not shown in Fig. 5 because we could not show definitive stability, as we could for ETG modes.

The difficulty is that the ballooning approximation is no longer valid at small values of magnetic shear, $\hat{s}=(r/q)(dq/dr)$, as in the plasma core (Fig. 2b). In this case, in the absence of strong driving forces, the eigenfunctions then become very broad and cannot be well resolved, and usually neglected higher-order corrections become important. Calculations with a full radius, global code such as GTC[29] or GYRO[30] could be used to resolve these modes and confirm ITG/TEM stability, as they do not make use of the ballooning approximation.

Figures 5a and 5b show that in the barrier region ($r/a \sim 0.45$) there are weak ITG/TEM modes for $0.1<k_\perp\rho_s<0.4$, while outside the ITB region ITG/TEM drift modes are strongly unstable at $0.1<k_\perp\rho_s<0.8$. The TEM mode (usually found near $k_\perp\rho_s \sim 1$) is stable everywhere. The ETG mode is strongly unstable at and outside the barrier, with maximum growth rates near $k_\perp\rho_s \sim 20$. Earlier gyrokinetic calculations[11,12] of this plasma assumed ion collisionalities whose ratios ($\nu_{d\text{-}i}/\nu_{e\text{-}i}$) were too high by factors of (36, 20, 6) for plasma radii (0.25, 0.45, 0.65). Such high ion collisionalities completely stabilized the weak ITG/TEM mode in the barrier region[11] and led to quiescent microturbulence in nonlinear simulations[12]. Ion collisionalities are corrected in the present work and in Ref. 13.

Figure 6 shows the eigenfunctions of the ITG/TEM electrostatic potential at and outside the ITB region for $k_\perp\rho_s$=0.2. The modes are well converged outside the plasma core.

At the ITB onset time the fastest growing ITG/TEM mode growth rates (0.0 MHz, 0.026 MHz, 0.13 MHz) increase with increasing radii, $r/a$=(0.25, 0.45, 0.65). In Fig. 7 are shown the most important dimensionless driving forces, which usually destabilize or stabilize ITG/TEM instabilities, at these values of $r/a$. The parameters $\eta^i=(\nabla T_i/T_i)/(\nabla n_e/n_e)$, $-a\nabla T_i/T_i$, $-a\nabla T_e/T_e$, and $\hat{s}$ increase with radius, $-a\nabla n_e/n_e$ decreases with radius, while $Z_{eff}$ is assumed constant and $T_i/T_e$ is nearly constant.

### D. Effects on ITB region instability of scaling $L_T$ and $L_n$

An extensive study was carried out to investigate the effects of scaling the normalized temperature and density gradients on long wavelength ITG/TEM stability for plasma conditions in the barrier region (Figs. 8-11). The inverse temperature and density scale lengths, for each species $j$, are defined by $L_{Tj}^{-1} = \nabla T_j/T_j$ and $L_{nj}^{-1} = \nabla n_j/n_j$. The identification of the fastest growing mode type (ITG-like or TEM-like) and stability/instability for each scaling calculation was mapped onto the dashed lines of Fig. 4 and determined the stability boundaries. The temperatures or density gradients for all species were scaled by the same multiplicative factor, and all other plasma conditions were held constant.

In the barrier region at ITB onset, the C-Mod plasma is above marginal stability (Fig. 4, green star). This base case exhibits weak ITG/TEM instability and is well above the critical value of the normalized temperature gradient for ITG destabilization, $R[\nabla T/T]_{crit}$ = 0.8 $R[\nabla T/T]_{exp}$=6.9, as determined from Fig. 8a. The maximum ITG growth rate in Fig. 8 increases linearly with scaling factors $S_T \equiv \nabla T_j/T_j\,/[\nabla T_j/T_j]_{exp}$ up to 4, applied to all species $j$. For $S_T \leq 2.5$ the growth rate spectrum $\gamma^{\mathrm{ITG/TEM}}(k_\perp\rho_s)$ has a parabolic shape, peaked at ~0.2-0.3$k_\perp\rho_s$ (Fig. 9a). Above the experimental normalized temperature gradient, the growth rate shows nonmonotonic behavior. The wave vector of the fastest growing mode switches between $k_\perp\rho_s$ = 0.2 and 0.3. At

$S_T$= 2.5, $\gamma(k_\perp \rho_s)$ is as high as that found for strong ITG/TEM turbulence outside the ITB region at $r/a$ = 0.65 (Fig. 5b), in physical units. For $S_T$ equal to 2.5 and 3 there are indications of TEM-like as well as ITG-like ITG/TEM instabilities, but without properly localized eigenfunctions for values of $k_\theta \rho_s \sim 0.8$. Above $S_T$ = 4, a different root at long wavelength (a kinetic ballooning mode, $k_\perp \rho_s = 0.1$) becomes the most unstable mode (Fig. 8b) and the maximum growth rates rise by an order of magnitude with broadened, nonparabolic spectra (not shown).

The ITG/TEM instability is robust at all values of the logarithmic density gradient multiplier $S_N$, (Figs. 10-11) changing from ITG-like to TEM-like with increasing scaling factors, as expected from the stability diagram of Ref. 28. The maximum growth rate increases linearly with $S_N$ up to multiplicative factor 4, becoming increasingly sensitive to the multiplicative factor above 6. The real frequency of the fastest growing mode decreases slowly up to scaling factor 4 and then at 6 the solution transitions from an ITG-like to a TEM-like root with tearing parity. Kinetic theory has shown in general that density peaking may stabilize or destabilize the ITG/TEM mode, depending on plasma collisionality, trapped electron fractions and $T_i/T_e$[31,32]. At ITB onset in the barrier region, density peaking further destabilizes the ITG/TEM mode in the C-Mod case, as is also found in Ref. 14. For the C-Mod ITB onset time, we find the growth rates in the barrier region are much more sensitive to increased temperature gradients than to increased density gradients and that there is no critical density gradient below which the ITG/TEM modes are stable.

## IV. DISCUSSION

Linear stability analysis of the C-Mod ITB at the onset time shows that long wavelength ITG/TEM modes are weakly unstable at the barrier region. This provides an environment with little plasma microturbulence and allows the Ware pinch to cause the density peaking seen in the

experiment[9,14]. Additional linear calculations were used to create an ITG/TEM drift mode stability phase diagram for this C-Mod plasma. We next compare the ITG stability threshold obtained for the barrier region to predictions from standard microstability models[20,28,33-35]. Such comparisons can verify the accuracy of the parametric dependencies of simpler, analytic or computationally-based models.

### A. Comparison with analytic models for the ITG stability threshold

The long wavelength drift mode phase diagram, Fig. 4, is in qualitative agreement with the original phase diagram[28]. Although the critical temperature gradient threshold in Fig. 4 for the barrier region $|R\nabla T/T|_{ITG/TEM}$ is 6.9 and in Ref. 28 this critical temperature gradient is 2.5, such a difference is not unexpected. The thresholds depend on all the plasma parameters, in addition to the density or temperature gradients being varied. Although all the C-Mod radii simulated are denoted on Fig. 4, only the topology of the stability plot is constant; the scales of the axes are set for simulations at $r/a$=0.45, and will be different for $r/a= 0.25$ and for $r/a= 0.65$. Figure 4 is based on electromagnetic GS2 calculations. Although GS2 identifies only the fastest growing modes at each wavelength, there may be many other modes present with weaker growth rates. In the figure, we also show the pressure-driven kinetic ballooning stability boundary. This stability boundary is roughly part of an ellipse determined by two transition points. Since it is a shear-Alfvenic oscillation with its stability boundary depending most strongly on $R\nabla T_i/T_i$, it is sometimes called an Alfvenic ion temperature gradient (AITG) instability[36].

We next compare GS2 results to a standard analytic model for the ITG stability threshold (see Ref. 20, page 403). At the onset time for ITB formation, the barrier region has a density profile sufficiently flat that the toroidal ITG mode threshold is described by a critical temperature

gradient, rather than a critical $\eta_i$. We find that the commonly quoted critical value $\eta_i^{crit} \cong 1.2$, for normal density profiles, is not valid for the ITG/TEM instability at the ITB onset time.

If $\varepsilon_n \equiv L_n/R > \varepsilon_n^{crit} = 0.9/[1+1/(T_e/T_i)][1+2\hat{s}/q]$, the density profile is broad enough that the critical parameter $\eta_i^{crit}$ becomes

$$\eta_i^{crit} = (4/3)[1+1/(T_e/T_i)][L_n/R][1+2\hat{s}/q]. \quad (1)$$

$L_n$ is the electron density scale length. At the ITB onset time for radii ($r/a$=0.25, 0.45, 0.65), $\varepsilon_n$ has the values (0.5, 0.8, 8.3), higher than the critical thresholds $\varepsilon_n^{crit}$, (0.22, 0.18, 0.17). Thus $\eta_i^{crit}$ is better approximated by the flat density regime formula given in Eq. (1), with the values (3.2, 5.6, 56) at these three plasma radii. Given these critical thresholds, the experimental values of $\eta_i$, (0.94, 6.5, 68) are well below criticality in the core, and above threshold in the ITB region and outside the ITB, and are in agreement with the linear gyrokinetic stability analysis. At 0.8 s we attribute quantitative differences between Eq. (1) and the gyrokinetic model threshold calculations to a positive (reversed) density gradient in the barrier region (Fig. 2a). Since $\eta_i^{crit} = [\nabla T_i/T_i]_{crit}/[\nabla n_e/n_e]_{exp}$, this standard model predicts $R[\nabla T_i/T_i]_{crit} = \eta_i^{crit}[\nabla n_e/n_e]_{exp} = 7.1$, close to the GS2 result.

Finally, we compare the GS2 ITG/TEM threshold obtained for the C-Mod ITB onset time to an analytic extension of a computationally-based model. Based on extensive linear GS2 calculations, Jenko[33] has formulated an algebraic ETG critical temperature gradient, which reduces to two previous analytic theories[34,35] for ITG/TEM modes in appropriate limits. This ETG critical temperature gradient formulation can be extended approximately to ITG/TEM modes if $\eta_i$ replaces $\eta_e$, $L_{Ti}$ replaces $L_{Te}$, and $T_i/T_e$ replaces $T_e/T_i$. Geometrical effects are likely to be the same for electrons and ions. We neglect $Z_{eff}$ dependence, as the role of $Z_{eff}$ is complex in

controlling the stability of ITG modes[37], as well as other small corrections. This transformation leads to an ITG critical temperature gradient threshold

$$R(\nabla T_i/T_i)_{crit} = \max\{(1+\tau)(1.33+1.91\,\hat{s}/q)\,(1-1.5\varepsilon)[1+0.3\varepsilon d\kappa/d\varepsilon)],\ 0.8R/L_n\}.$$

In the barrier region $q$=1.32, $\hat{s}$=0.96, $\tau \equiv T_i/T_e = 1.16$, $\kappa = 1.24$, $\varepsilon \equiv r/R_o = 0.14$ and $(\varepsilon/\kappa)(d\kappa/d\varepsilon) = 0.08$. $\kappa$ denotes the elongation. The critical ion temperature gradient from our linear calculations of the barrier region at ITB onset, $(R/L_{Ti})_{\rm crit}$ =6.9, is 40% higher than that predicted by the above formula, 4.9. Our calculations were based on numerical equilibria and include geometrical effects as in the standard ETG model[24], but also include trapped particle effects, complete FLR effects, electron-ion collisions and impurity ions. The difference in critical temperature gradients might suggest that the transport barrier is more easily formed near $r/a$=0.45 than for typical high turbulence plasma regions which were the basis of the critical temperature gradient models, but a 40% difference between the GS2 threshold and our extension of the Jenko threshold is not unexpected. Trapped particle effects, electron-ion collisions and impurity ions are likely to be important in accurately modeling ITB formation, and we encourage future gyrokinetic simulations to include these effects in developing improved algebraic critical gradient models.

### B. Comparison of gyrokinetic modeling to transport analysis of experiment

In principle, predictions for experimentally measured heat and particle fluxes and transport coefficients can be found for each plasma species. However, because C-Mod has such high plasma density, error estimates for electron or ion heat fluxes and diffusivities can be as large as ±70%, so that the effective heat transport coefficient

$$\chi_{eff} = (\chi_i n_i \nabla T_i + \chi_e n_e \nabla T_e)/(n_i \nabla T_i + n_e \nabla T_e)$$

is reported, rather than $\chi_e$ and $\chi_i$. In Fig. 12 the experimental $\chi_{eff}$ and the neoclassical ion thermal conductivity[18], $\chi_i^{Chang\text{-}Hinton}$, are shown at the ITB onset time. The large differences between the experimental effective heat diffusivity and $\chi_i^{Chang\text{-}Hinton}$, both at and outside the ITB region, mean that microturbulent-based anomalous transport is likely to be important at both locations.

Waltz[38] discusses the difficult task of reducing complex, nonlinear simulation results into an algebraic formula for predictive transport coefficients. We have estimated ITG/TEM-driven mixing length transport coefficients from the linear calculations according to the simple formulation: $\chi_{mix} = \gamma^{ITG/TEM}/\langle k_\perp^2 \rangle$, where <…> indicates a field line average and the wave vector is chosen at maximum growth rate $\gamma^{ITG/TEM}$. These estimates are compared to $\chi_{eff} - \chi_i^{Chang\text{-}Hinton}$ for the three plasma radii in Table II. This simple mixing length formulation is in agreement with transport analysis in the plasma core and overestimates the observed transport by less than a factor of two at and outside the barrier region. This is relatively good agreement with experiment for the linear calculations.

Generally nonlinear simulations are desired for model validation against experiment. However, it is unlikely that nonlinear gyrokinetic calculations will yield significant ITG/TEM microturbulence in the core, given the flat density and temperature profiles and no strongly growing linear instabilities. Subcritical turbulence has only been identified in gyrofluid calculations near the plasma edge[39]. Self-sustained core drift wave turbulence has not been observed to date at the low collisionality,

$$C = 0.51 \frac{\nu_e L_{Te}}{c_s} \frac{m_e}{m_d} \left( \frac{qR}{L_{Te}} \right)^2 \sim 10^{-3} << 1.$$

$\nu_e$ is the electron collision frequency. Nonlinear calculations would be needed for better benchmarking of the gyrokinetic model against experiment at and outside the ITB region at the

onset time. Such calculations for TEM[14] are found to be in rough agreement with transport analysis of the barrier region later in this experiment during the fully developed ITB phase. Fully converged nonlinear simulations of both ITG/TEM and ETG modes are needed, since it is not known how energy losses are divided between the electron and ion channels in C-Mod.

## V. CONCLUSION

Fully electromagnetic, linear, gyrokinetic calculations of the Alcator C-Mod ITB during off-axis rf heating, following four plasma species and including the complete electron response show ITG/TEM microturbulence is suppressed in the plasma core and in the barrier region before barrier formation, without recourse to the usual requirements of velocity shear or reversed magnetic shear. No strongly growing long or short wavelength drift modes are found in the plasma core but strong ITG/TEM and ETG drift wave turbulence is found outside the barrier region. Linear microstability analysis is qualitatively consistent with the experimental transport analysis, showing low transport inside and high transport outside the ITB region before barrier formation, without consideration of ***ExB*** shear effects.

Since there are no strong ITG/TEM drift wave instabilities at the ITB region, microturbulent driving forces are not strong enough to provide outward anomalous particle transport across the barrier region even before ITB formation. The good confinement appears to result from a combination of factors in the ITB region ($q$, $\hat{s}$, $-\nabla n/n$, $-\nabla T/T$), which are not sufficient to stabilize turbulent microstabilities outside the plasma core. The strong dependence of the barrier region ITG/TEM instability on the normalized temperature gradient suggests that local rf heating may underlie ITB formation in this experiment. Further experimental and computational tests will be needed to identify trigger mechanisms for the C-Mod ITB. Comparison of computational models to analytic models and experiment are essential in

establishing credibility for computational physics. We find standard analytic models of the ITG/TEM critical temperature gradient threshold compare satisfactorily to the GS2 gyrokinetic model and that the ITG/TEM mixing length model is roughly consistent with experiment at ITB onset.

## ACKNOWLEDGEMENT

We are glad to acknowledge the experimental and diagnostic teams at Alcator C-Mod. J. Baumgaertel, a student at University of Washington, Seattle, held a Science Undergraduate Laboratory Internship (SULI) at the Princeton Plasma Physics Laboratory during the summer of 2004. Her SULI paper was selected to appear in the DoE Journal of Undergraduate Research (Ref. 16). Contributions by D. Ernst, MIT, to the early stages of this work are gratefully acknowledged. We especially wish to acknowledge stimulating discussions about the experiment with P. Bonoli, M. Greenwald, A. Hubbard, B. Lipschultz, J. Rice, J. Terry, S. Wolfe, and S. Wukitch at MIT and about microinstability physics and plasma and gyrokinetic modeling with R. Budny, K. Hill, D. McCune, D. Mikkelsen and W. Lee of Princeton Plasma Physics Laboratory, Princeton University, with C. Bourdelle, Euratom-CEA, France and with F. Jenko and B. Scott, Max-Planck-Institut fur Plasmaphysik, EURATOM, Garching, Germany. We also thank G. Schilling, PPPL, and E. Marmar and M. Porkolab, MIT, for their encouragement and support. Research was carried out under U. S. DOE Contract DE-AC02-76CH03073.

**References**


[1] I. H. Hutchinson, R. L. Boivin, F. Bombarda *et al*., Phys. Plas. **1**, 1511 (1994).

[2] "ITER Physics Basis", Nuclear Fusion **39,** 2137-2638 (1999).

[3] M. Kotschenreuther, G. Rewoldt and W. M. Tang, Comp. Phys. Comm. **88**, 128 (1995).

[4] W. Dorland, F. Jenko, M. Kotschenreuther and B. N. Rogers, Phys. Rev. Lett. **85**, 5579 (2000). The GS2 website may be found at http://gs2.sourceforge.net

[5] C. L. Fiore, J. E. Rice, P. T. Bonoli, *et al*., Phys. Plas. **8,** 2023 (2001).

[6] R. C. Wolf, Plasma Physics and Controlled Fusion **45,** R1-R91 (2003).

[7] S. Wukitch, R. L. Boivin, P. T. Bonoli, *et al.,* Phys. Plas. **9**, 2149 (2002).

[8] J. E. Rice, P. T. Bonoli, E. Marmar, *et al.,* Nuclear Fusion **42,** 510 (2002).

[9] C. L. Fiore, P. T. Bonoli, D. R. Ernst, *et al*., Phys. Plas. **11,** 2480 (2004).

[10] C. L. Fiore, P. T. Bonoli, D. R. Ernst, *et al*., Plasma Physics and Controlled Fusion **46,** B281-291 (2004).

[11] M. H. Redi*,* C. Fiore, P. Bonoli*, et al*., Proceedings of the 29th EPS Conference on Plasma Physics and Controlled Fusion, Montreux, Switzerland, 2002, edited by R. Behm, C. Varandas (European Physical Society, Lausanne, 2002), Vol. **26B**, Paper 1.082.

[12] M. H. Redi, R. Bell, P. Bonoli *et al*., Proceedings of the 30th EPS Conference on Plasma Physics and Controlled Fusion, St. Petersburg, Russia, 2003, edited by R. Koch, S. Lebedev (European Physical Society, Lausanne, 2003), Vol. **27A**, Paper P4.94.

[13] M. H. Redi, C. L. Fiore, W. Dorland, *et al.,* Proceedings of the 31th EPS Conference on Plasma Physics and Controlled Fusion, London, England, 2004, (European Physical Society, Lausanne, 2004), Vol. **28G**, Paper P2-163.

[14] D. R. Ernst, P. T. Bonoli, P. J. Catto*, et al*., Phys. Plas. **11,** 2637 (2004).

[15] J. E. Rice, P. T. Bonoli, C. L. Fiore, *et al.,* Nuclear Fusion **43,** 781 (2003).

[16] J. A. Baumgaertel, M. H. Redi, R. V. Budny, *et al*., "Marginal stability studies of microturbulence near ITB onset on Alcator C-Mod", to appear in the electronic journal U.S. Department of Energy Office of Science Journal of Undergraduate Research, Vol. **5** (2005). www.scied.science.doe.gov/scied/JUR.html

[17] R. J. Hawryluk, in *Physics of Plasmas Close to Thermonuclear Conditions*, edited by B. Coppi, G. G. Leotta, D. Pfirsch, R. Pozzoli, and E. Sindoni (Pergamon, Oxford, 1980), Vol. 1, p. 19.

[18] C. S. Chang and F. L. Hinton, Phys. Fluids **25**, 1493 (1982).

[19] D. McCune, G. W. Hammett and C. Bourdelle, private communication (2002). TRXPL is available at w3.pppl.gov/NTCC; contact D. McCune, dmccune@pppl.gov.

[20] J. A. Wesson, *Tokamaks,* Oxford University Press, New York, NY (1997), chapters 2 and 8.

[21] W. Horton, Rev. Mod. Phys. **71,** 735 (1999).

[22] G. Rewoldt, W. M. Tang and M. S. Chance, Phys. Fluids **25**, 480 (1982).

[23] B. Coppi and G. Rewoldt, in *Advances in Plasma Physics*, edited by A. Simon and W. B. Thompson (John Wiley and Sons, New York, 1976), Vol**. 6**, p. 421.

[24] Y. C. Lee, J. Q. Dong, P. N. Gudar *et al*., Phys. Fluids **30**, 1331 (1987).

[25] P. N. Guzdar, C. S. Liu, J. Q. Dong *et al.*, Phys. Rev. Lett. **57**, 2818 (1986).

[26] W. Horton, B. G. Hong and W. M. Tang, Phys. Fluids **31**, 2971 (1988).

[27] H. Biglari and P. H. Diamond, Phys. Fluids **B3**, 1797 (1991).

[28] X. Garbet, P. Mantica, C. Angioni, *et al.*, Plasma Physics and Controlled Fusion **46,** B557-B574 (2004).

[29] Z. Lin, T. S. Hahm, W. W. Lee, *et al.*, Science **281**, 1835 (1998).

[30] R. E. Waltz, J. M. Candy and M. N. Rosenbluth, Phys. Plas. **9**, 1938 (2002).

[31] F. Zonca, L. Chen, R. A. Santoro and J. Q. Dong, Phys. Plas. **6**, 1917 (1999).

[32]F. Romanelli and S. Briguglio, Phys. Fluids **B2,** 754 (1990).

[33] F. Romanelli, C. Bourdelle and W. Dorland, Phys. Plas. **11**, 3845 (2004).

[34] F. Jenko, W. Dorland and G. W. Hammett, Phys. Plas**. 8**, 4096 (2001).

[35] F. Romanelli, Phys. Fluids **B1**, 1018 (1989)

[36] T. S. Hahm and W. M. Tang, Phys. Fluids **B1**, 1185 (1989).

[37] M. Kotschenreuther, W. Dorland, M. Beer and G. W. Hammett, Phys. Plas. **2**, 2381 (1995).

[38] R. E. Waltz, G. M. Staebler, W. Dorland, *et al.*, Phys. Plas. **4** , 2482 (1997).

[39] B. D. Scott, Plasma Phys. Control. Fusion **45**, A385-A398 (2003).

Table I. Plasma parameters for C-Mod gyrokinetic calculations at 0.9 sec.

| Parameter | $r/a$ | 0.25 | 0.45 | 0.65 |
|---|---|---|---|---|
| $q$ | | 0.99 | 1.32 | 2.00 |
| $\hat{s}$ | | 0.51 | 0.96 | 1.48 |
| $T_d/T_e = T_b/T_e$ | | 0.99 | 1.16 | 1.06 |
| $T_h/T_e$ | | 1.30 | 3.96 | 1.59 |
| $-a_{ref}\nabla n_e/n_e = -a_{ref}\nabla n_d/n_d$ | | 0.71 | 0.42 | 0.04 |
| $-a_{ref}\nabla n_b/n_b$ | | 0.71 | 0.43 | 0.05 |
| $-a_{ref}\nabla n_h/n_h$ | | 0.71 | 0.42 | 0.04 |
| $-a_{ref}\nabla T_e/T_e$ | | 1.47 | 2.35 | 2.83 |
| $-a_{ref}\nabla T_d/T_d = -a_{ref}\nabla T_b/T_b$ | | 0.67 | 2.75 | 3.41 |
| $-a_{ref}\nabla T_h/T_h$ | | -3.13 | 15.4 | 5.69 |
| $\nu_{e\text{-}i}\, a_{ref}/(c_s\sqrt{2})$ | | 0.30 | 0.56 | 1.54 |
| $\nu_{d\text{-}i}\, a_{ref}/(c_s\sqrt{2})$ | | 0.01 | 0.02 | 0.05 |
| $\nu_{b\text{-}i}\, a_{ref}/(c_s\sqrt{2})$ | | 0.07 | 0.11 | 0.33 |
| $\nu_{h\text{-}i}\, a_{ref}/(c_s\sqrt{2})$ | | 0.01 | 0.01 | 0.04 |
| $T_{ref} = T_e$ (keV) | | 1.15 | 0.77 | 0.45 |
| $n_{ref} = n_e$ ($10^{20}$m$^{-3}$) | | 3.1 | 2.8 | 2.7 |
| $\beta_{ref}$ (%) | | 0.75 | 0.45 | 0.25 |
| $c_s=(T_{ref}/m_{ref})^{0.5}$ ($10^4$ m/sec) | | 24. | 19. | 15. |
| Freq norm= $c_s/a_{ref}$ (MHz) | | 1.07 | 0.88 | 0.67 |

Table II. Comparison of linear ITG/TEM mixing length model transport coefficients to anomalous transport coefficients, $\chi_{eff}$-$\chi_i^{Chang\text{-}Hinton}$, derived from transport analysis of experiment.

| *r/a* | 0.25 | 0.45 | 0.65 |
|---|---|---|---|
| $\chi_{mix} = \gamma^{ITG/TEM}/\langle k_\perp^2 \rangle$ $(m^2/s)$ | 0 | 0.76 | 1.04 |
| $\chi_{eff}$-$\chi_i^{Chang\text{-}Hinton}$ $(m^2/s)$ | 0 | 0.4 | 0.8 |

**Figure Captions**

Figure 1. C-Mod ITB discharge with off-axis ICRF heating throughout the discharge and central ICRF heating applied after the ITB is established. Summary traces are ICRF power, stored plasma energy, line-averaged density, neutron rate, central ion temperature and toroidal rotation. Figure reproduced from Ref. 7, used with permission of the author.

Figure 2. a) Radial profiles of electron density showing evolution from L-mode (0.7 s) to H-mode (0.8, 0.9 s) and the ITB development phase, with peaked density profiles at times up to 1.2 s. The times of interest are 0.8 and 0.9 s, before the ITB is established. The three radial locations shown, $r/a$~0.25, 0.45 and 0.65, are chosen to represent conditions in the plasma core, the ITB barrier region and outside the ITB region. b) Radial profiles of the plasma safety factor, $q$, from 0.7 to 1.2 s. The profile $q(r)$ for 0.9 s is also inset separately. c) Electron temperature profiles for times from 0.7 to 1.2 s. d) Ion temperature profiles for times from 0.7 to 1.2 s.

Figure 3. The growth rates (a) and real frequencies (b) of the ITG/TEM modes in the ITB region at 0.8 s and 0.9 s are nearly identical, although the plasma densities differ.

Figure 4. Phase diagram for linear instability of ITG and TEM drift modes for the C-Mod plasma before ITB formation. Diagram adapted from Figure 1 of Ref. 28. Star symbols indicate three C-Mod radial locations simulated, with stable conditions found in the plasma core (red), weakly unstable ITG instability at the barrier region (green) and strongly unstable ITG mode outside the barrier region (blue). Dashed lines map locations for linear simulations carried out to study the effect of variations in density and temperature gradients about the base case at the barrier region. $R\nabla T/T \equiv (R\nabla T_i/T_i + R\nabla T_e/T_e)/2$. $R\nabla N/N \equiv (R\nabla n_d/n_d + R\nabla n_e/n_e)/2$. $R$ is the major radius. The kinetic ballooning stability threshold is represented by part of an ellipse.

Figure 5. a) Linear instability growth rates in the plasma core, and at and outside the ITB for $k_\perp \rho_s$ from 0.1 to 80, the ITG/TEM and ETG range of wave numbers. b) Growth rates in the long wavelength ITG/TEM range are shown on a linear wave number scale. At the time of onset, there are no strongly growing ITG/TEM modes in the plasma core, only weak instabilities at the barrier region and strong ITG/TEM instabilities outside the barrier region. c) Real frequencies in the plasma core, and at and outside the barrier region for $k_\perp \rho_s$ from 0.1 to 80, the ITG/TEM and ETG range of drift mode wave vectors.

Figure 6. Real and imaginary parts of the electrostatic eigenfunctions of the $k_\perp \rho_s$=0.2 ITG/TEM drift wave modes for a) the ITB region where $\gamma^{ITG/TEM}_{max}$=0.026 MHz and b) outside the ITB region where $\gamma^{ITG/TEM}_{max}$=0.13 MHz. No unstable, well converged ITG/TEM mode is found in the plasma core.

Figure 7. The normalized driving forces ($-a\nabla T_i/T_i$, $-a\nabla T_e/T_e$, $Z_{eff}$, $T_i/T_e$, $\hat{s}$, $-a\nabla n_e/n_e$, $\eta_i \equiv [\nabla T_i/T_i]/[\nabla n_e/n_e]$) known to most strongly stabilize or destabilize long wavelength drift mode microturbulence, are shown at ITB onset for three plasma radii at 0.9 sec.

Figure 8. (a) Maximum ITG/TEM growth rates in the barrier region increase with scaling factors $S_T$ up to 2. For each species $j$, the normalized temperature gradient is scaled by the same factor $S_T$, $\nabla T_j/T_j = S_T[\nabla T_j/T_j]_{exp}$. The barrier region is slightly above marginal stability before barrier formation: the ITG instability threshold is 0.8 × the normalized logarithmic derivative of the experimental temperature. (b) Maximum ITG/TEM growth rates increase with temperature gradient scaling factors $S_T$ up to 8. A new root, a kinetic ballooning mode, is destabilized at $S_T$ = 5.

Figure 9. a) The growth rate spectra $\gamma^{ITG/TEM}(k_\perp \rho_s)$ at long wavelength in the barrier region at ITB onset time exhibit increasing maximum growth rates for scaling factors $S_T$ up to 2. b) The drift

mode real frequencies $\omega^{ITG/TEM}(k_\perp \rho_s)$ at long wavelength are predominantly ITG-like, rotating in the ion diamagnetic direction for $S_T$ up to 3.

Figure 10. a) The maximum ITG/TEM growth rate dependence on scaled density gradients. Each species is scaled by the same normalized density gradient scaling factor, $S_N \equiv (\nabla n_j/n_j)/[\nabla n_j/n_j]_{exp}$. The fastest growing mode changes from ITG-like to TEM-like near scaling factor 6. b) Real frequencies corresponding to the maximum growth rates of the ITG/TEM modes for scaling factors $S_N \equiv (\nabla n_j/n_j)/[\nabla n_j/n_j]_{exp}$ up to 10.

Figure 11. a) Spectra of ITB region growth rates $\gamma^{ITG/TEM}(k_\perp \rho_s)$ for density gradient scaling factors $S_N \equiv (\nabla n_j/n_j)/[\nabla n_j/n_j]_{exp}$ up to 10. b) Real frequencies $\omega^{ITG/TEM}(k_\perp \rho_s)$ for scaling factors $S_N \equiv (\nabla n_j/n_j)/[\nabla n_j/n_j]_{exp}$ . For scaling factors greater than 5-6, the modes are TEM-like at low values of $k_\perp \rho_s$, with the real frequency in the electron diamagnetic direction.

Figure 12. Radial profiles of $\chi_{eff}$ and the Chang-Hinton neoclassical ion conductivity from transport analysis of the experiment at 0.9 s. Anomalous transport must be accounted for outside $r/a$=0.25 and may correspond to unstable ITG/TEM and ETG drift mode microturbulence.

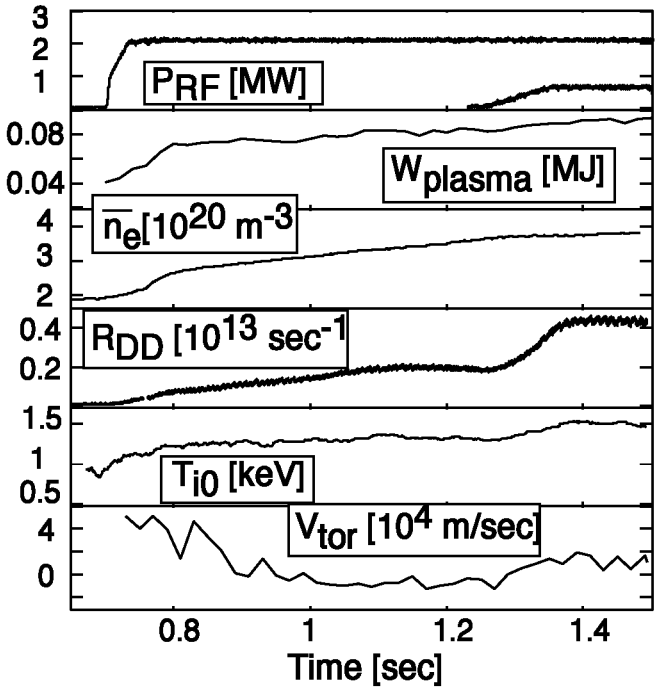
3
2
1
$P_{RF}$ [MW]
0.08
0.04
$W_{plasma}$ [MJ]
$\bar{n}_e[10^{20}\ m^{-3}]$
4
3
2
0.4
0.2
$R_{DD}$ [$10^{13}$ $sec^{-1}$]
1.5
1
0.5
$T_{i0}$ [keV]
4
0
$V_{tor}$ [$10^4$ m/sec]
0.8
1
1.2
1.4
Time [sec]

Redi
Fig. 1

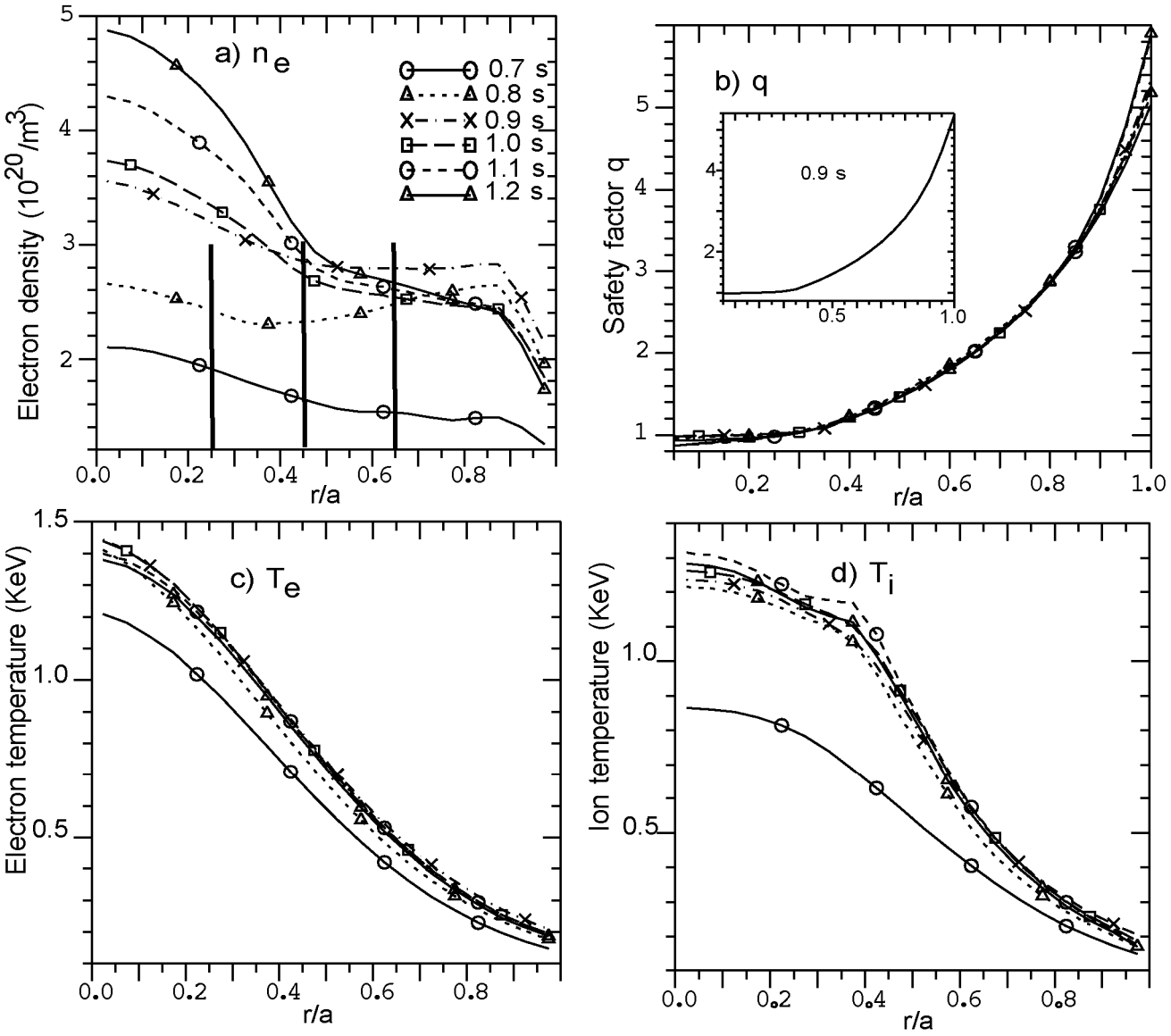
a) $n_e$
0.7 s
0.8 s
0.9 s
1.0 s
1.1 s
1.2 s
Electron density ($10^{20}$/m$^3$)
r/a
b) q
0.9 s
Safety factor q
r/a
c) $T_e$
Electron temperature (KeV)
r/a
d) $T_i$
Ion temperature (KeV)
r/a

Fig. 2, Redi

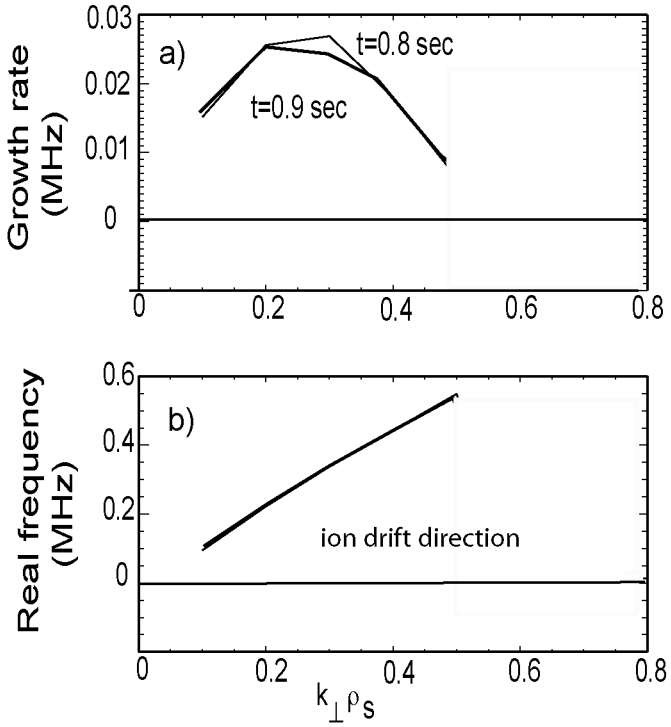
Growth rate (MHz)
0.03
0.02
0.01
0
a)
t=0.8 sec
t=0.9 sec
0
0.2
0.4
0.6
0.8
Real frequency (MHz)
0.6
0.4
0.2
0
b)
ion drift direction
0
0.2
0.4
0.6
0.8
$k_\perp \rho_s$

Fig 3

Redi

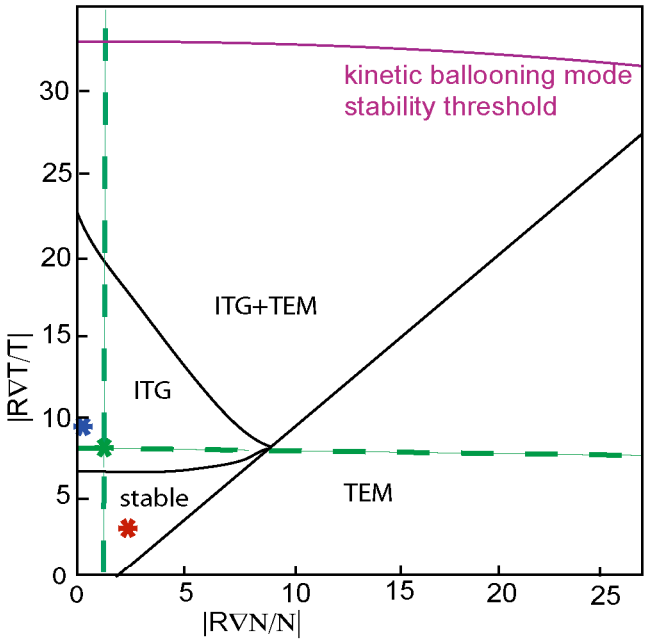
kinetic ballooning mode
stability threshold
ITG+TEM
ITG
stable
TEM
|RVT/T|
|RVN/N|
0
5
10
15
20
25
30

Redi
Fig. 4

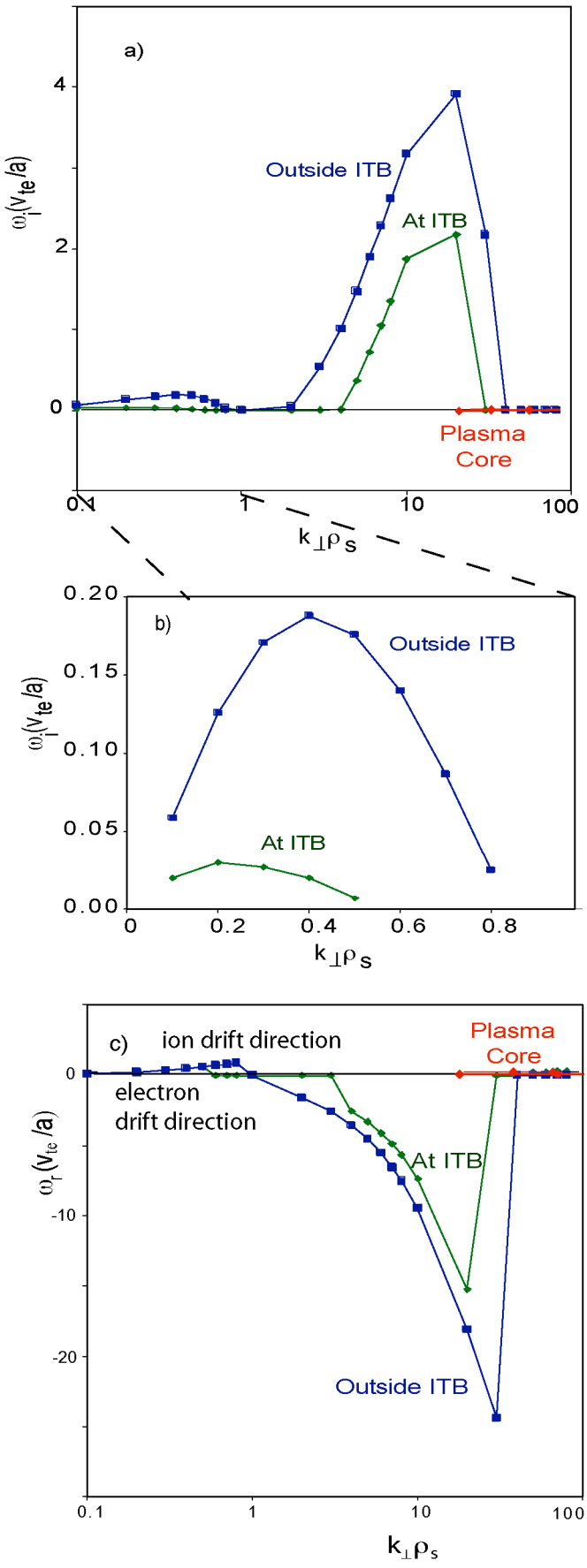
a)
Outside ITB
At ITB
Plasma
Core
$\omega_i(v_{te}/a)$
$k_\perp\rho_s$
b)
Outside ITB
At ITB
$\omega_i(v_{te}/a)$
$k_\perp\rho_s$
c)
ion drift direction
electron
drift direction
Plasma
Core
At ITB
Outside ITB
$\omega_r(v_{te}/a)$
$k_\perp\rho_s$

Fig 5

Redi

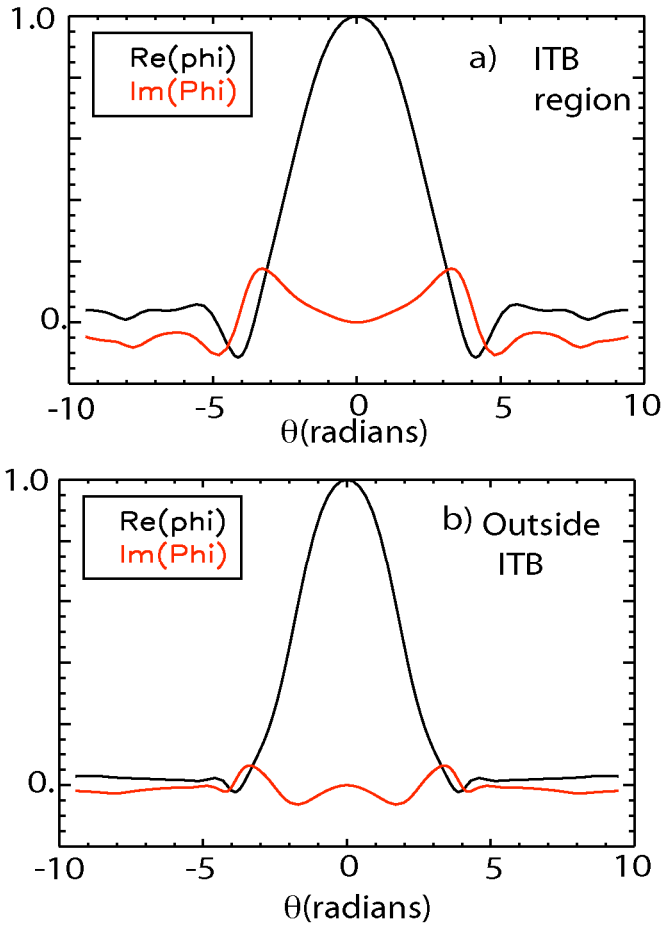
1.0
Re(phi)
Im(Phi)
a) ITB
region
0.
-10
-5
0
5
10
θ(radians)
1.0
Re(phi)
Im(Phi)
b) Outside
ITB
0.
-10
-5
0
5
10
θ(radians)

Fig.6
Redi

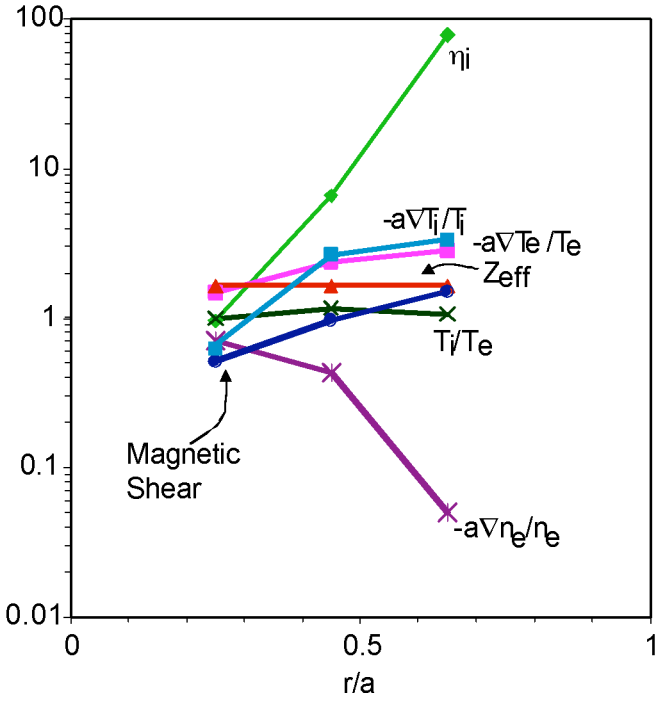
100
10
1
0.1
0.01
0
0.5
1
r/a
ηi
-aVTi/Ti
-aVTe/Te
Zeff
Ti/Te
Magnetic
Shear
-aVne/ne

Fig. 7
Redi

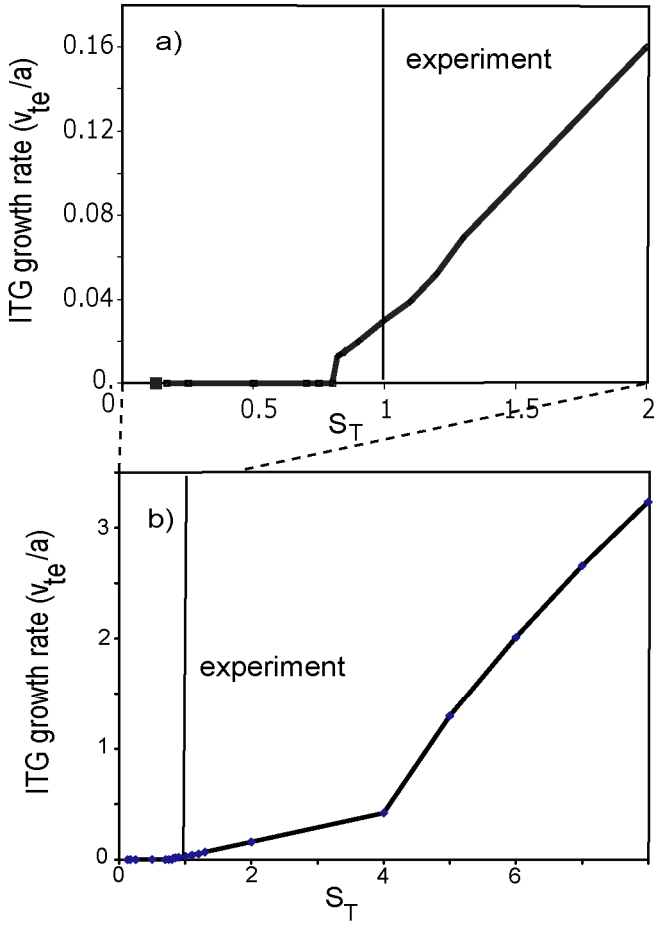
a)
experiment
ITG growth rate ($v_{te}/a$)
0.16
0.12
0.08
0.04
0
0
0.5
1
1.5
2
$S_T$
b)
experiment
ITG growth rate ($v_{te}/a$)
3
2
1
0
0
2
4
6
$S_T$

Fig 8

Redi

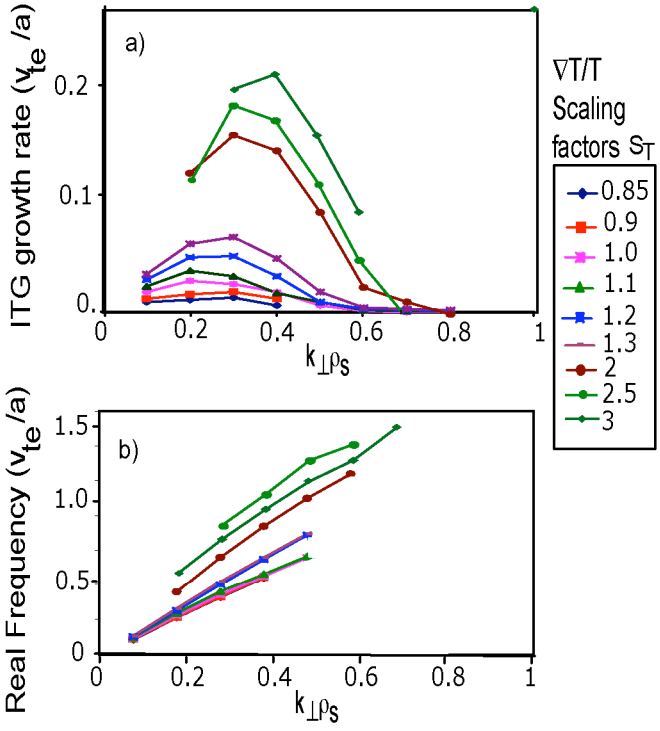
a)
ITG growth rate ($\gamma_{te}/a$)
0.2
0.1
0.
0
0.2
0.4
0.6
0.8
1
$k_\perp\rho_s$
∇T/T
Scaling
factors $S_T$
0.85
0.9
1.0
1.1
1.2
1.3
2
2.5
3
b)
Real Frequency ($\omega_{te}/a$)
1.5
1.0
0.5
0
0.2
0.4
0.6
0.8
1
$k_\perp\rho_s$

Fig. 9
Redi

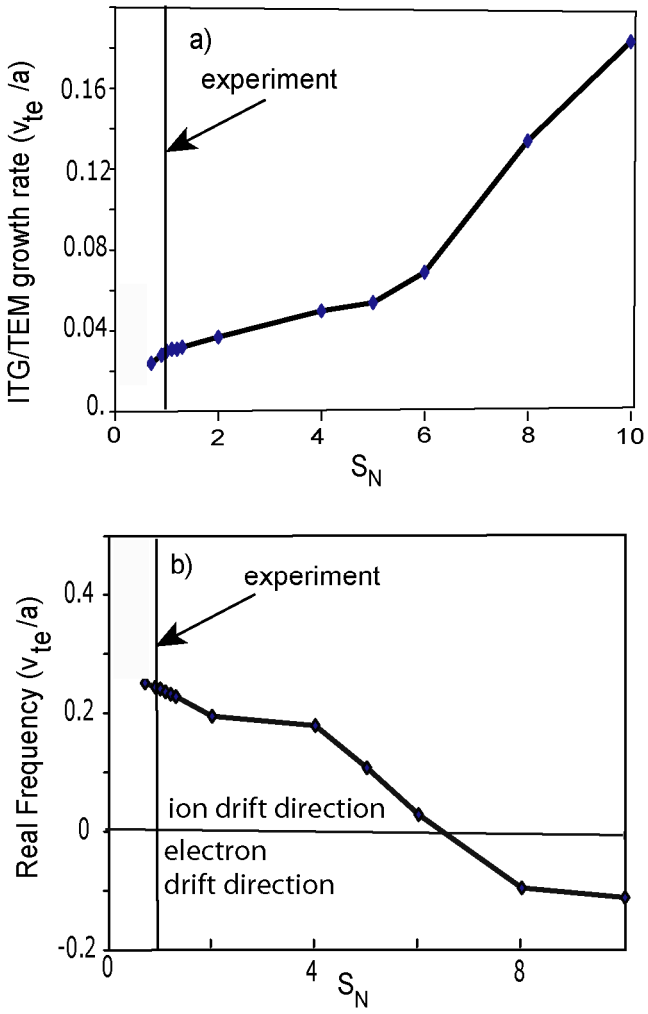
a)
experiment
ITG/TEM growth rate ($v_{te}/a$)
0.16
0.12
0.08
0.04
0.
0
2
4
6
8
10
$S_N$
b)
experiment
Real Frequency ($v_{te}/a$)
0.4
0.2
0
-0.2
ion drift direction
electron
drift direction
0
4
8
$S_N$

Fig. 10

Redi

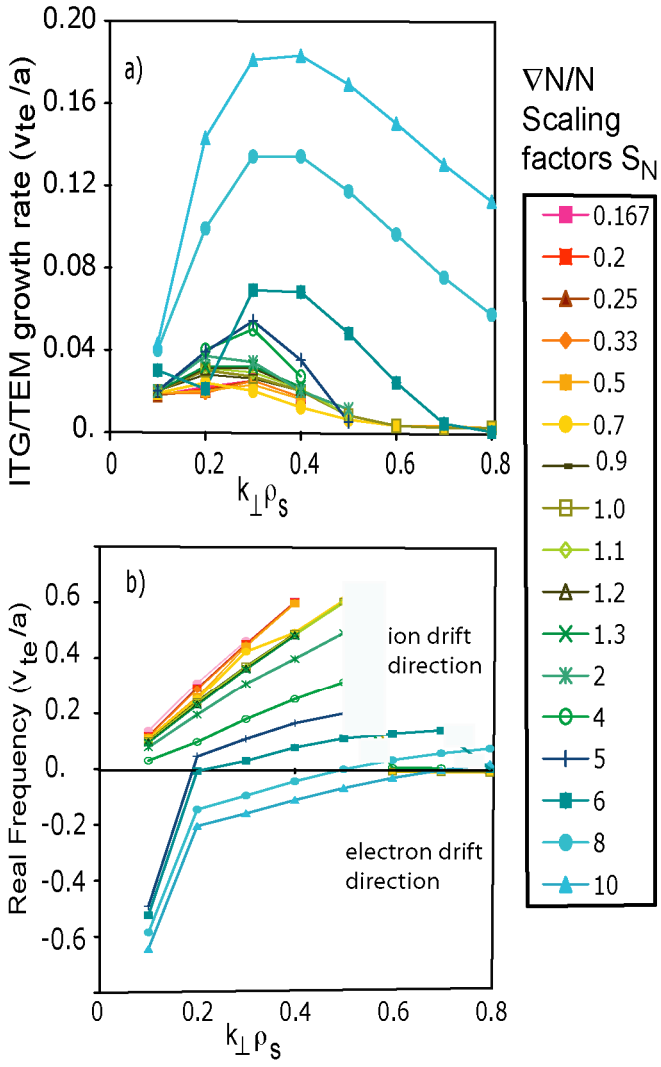
a)
ITG/TEM growth rate (vte /a)
0.20
0.16
0.12
0.08
0.04
0.
0
0.2
0.4
0.6
0.8
k⊥ρs
∇N/N
Scaling
factors SN
0.167
0.2
0.25
0.33
0.5
0.7
0.9
1.0
1.1
1.2
1.3
2
4
5
6
8
10
b)
Real Frequency (v te /a)
0.6
0.4
0.2
0.
-0.2
-0.4
-0.6
ion drift
direction
electron drift
direction
0
0.2
0.4
0.6
0.8
k⊥ρs

Fig 11

Redi

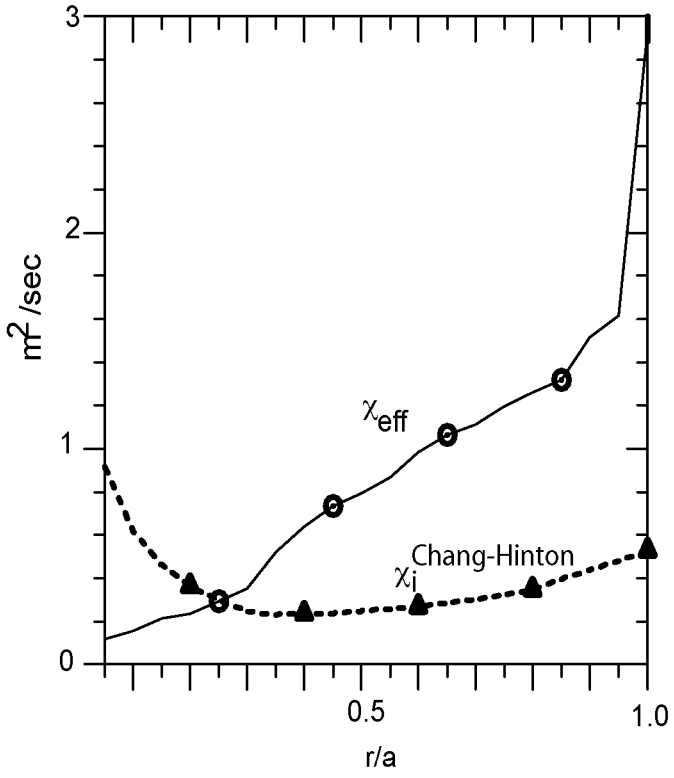


Fig. 12

Redi

# External Distribution

Plasma Research Laboratory, Australian National University, Australia
Professor I.R. Jones, Flinders University, Australia
Professor João Canalle, Instituto de Fisica DEQ/IF - UERJ, Brazil
Mr. Gerson O. Ludwig, Instituto Nacional de Pesquisas, Brazil
Dr. P.H. Sakanaka, Instituto Fisica, Brazil
The Librarian, Culham Science Center, England
Mrs. S.A. Hutchinson, JET Library, England
Professor M.N. Bussac, Ecole Polytechnique, France
Librarian, Max-Planck-Institut für Plasmaphysik, Germany
Jolan Moldvai, Reports Library, Hungarian Academy of Sciences, Central Research Institute for Physics, Hungary
Dr. P. Kaw, Institute for Plasma Research, India
Ms. P.J. Pathak, Librarian, Institute for Plasma Research, India
Dr. Pandji Triadyaksa, Fakultas MIPA Universitas Diponegoro, Indonesia
Professor Sami Cuperman, Plasma Physics Group, Tel Aviv University, Israel
Ms. Clelia De Palo, Associazione EURATOM-ENEA, Italy
Dr. G. Grosso, Instituto di Fisica del Plasma, Italy
Librarian, Naka Fusion Research Establishment, JAERI, Japan
Library, Laboratory for Complex Energy Processes, Institute for Advanced Study, Kyoto University, Japan
Research Information Center, National Institute for Fusion Science, Japan
Professor Toshitaka Idehara, Director, Research Center for Development of Far-Infrared Region, Fukui University, Japan
Dr. O. Mitarai, Kyushu Tokai University, Japan
Mr. Adefila Olumide, Ilorin, Kwara State, Nigeria
Dr. Jiangang Li, Institute of Plasma Physics, Chinese Academy of Sciences, People's Republic of China
Professor Yuping Huo, School of Physical Science and Technology, People's Republic of China
Library, Academia Sinica, Institute of Plasma Physics, People's Republic of China
Librarian, Institute of Physics, Chinese Academy of Sciences, People's Republic of China
Dr. S. Mirnov, TRINITI, Troitsk, Russian Federation, Russia
Dr. V.S. Strelkov, Kurchatov Institute, Russian Federation, Russia
Kazi Firoz, UPJS, Kosice, Slovakia
Professor Peter Lukac, Katedra Fyziky Plazmy MFF UK, Mlynska dolina F-2, Komenskeho Univerzita, SK-842 15 Bratislava, Slovakia
Dr. G.S. Lee, Korea Basic Science Institute, South Korea
Dr. Rasulkhozha S. Sharafiddinov, Theoretical Physics Division, Insitute of Nuclear Physics, Uzbekistan
Institute for Plasma Research, University of Maryland, USA
Librarian, Fusion Energy Division, Oak Ridge National Laboratory, USA
Librarian, Institute of Fusion Studies, University of Texas, USA
Librarian, Magnetic Fusion Program, Lawrence Livermore National Laboratory, USA
Library, General Atomics, USA
Plasma Physics Group, Fusion Energy Research Program, University of California at San Diego, USA
Plasma Physics Library, Columbia University, USA
Alkesh Punjabi, Center for Fusion Research and Training, Hampton University, USA
Dr. W.M. Stacey, Fusion Research Center, Georgia Institute of Technology, USA
Director, Research Division, OFES, Washington, D.C. 20585-1290

The Princeton Plasma Physics Laboratory is operated
by Princeton University under contract
with the U.S. Department of Energy.

Information Services
Princeton Plasma Physics Laboratory
P.O. Box 451
Princeton, NJ 08543

Phone: 609-243-2750
Fax: 609-243-2751
e-mail: pppl_info@pppl.gov
Internet Address: http://www.pppl.gov